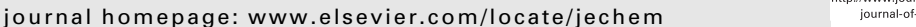


Contents lists available at ScienceDirect

### Journal of Energy Chemistry





ttp://www.journals.elsevier.com/

## PdNi/N-doped graphene aerogel with over wide potential activity for formic acid electrooxidation

Yufei Bao a,b, Meng Zha a,b, Pengliang Sun a, Guangzhi Hu a,\*, Ligang Feng b,\*

<sup>a</sup> School of Chemical Science and Technology and Institute for Ecological Research and Pollution Control of Plateau Lakes, Yunnan University, Kunming 650504, Yunnan, China <sup>b</sup> School of Chemistry and Chemical Engineering, Yangzhou University, Yangzhou 225002, Jiangsu, China

#### ARTICLE INFO

# Article history: Received 28 November 2020 Revised 13 December 2020 Accepted 13 December 2020 Available online 31 December 2020

Keywords: Fuel cells Formic acid oxidation reaction PdNi Graphene aerogel

#### ABSTRACT

Anti-CO poisoning ability is significant in formic acid oxidation in the fuel cell technique. Herein, PdNi alloy supported on N-doped graphene aerogel (PdNi/GA-N) was found to have catalytic ability toward formic acid electrooxidation over a wide potential range because of the improved anti-CO poisoning ability. This catalyst was fabricated by simple freeze-drying of mixture solution of graphene aerogel, polyvinylpyrrolidone,  $Pd^{2+}$  and  $Ni^{2+}$  and the subsequent thermal annealing reduction approach in the  $N_2/H_2$  atmosphere. Pd–Ni alloy particles anchored over the folding N-doped graphene surface with a porous hierarchical architecture structure in the 3D directions. It showed the catalytic performance of its maximum mass activity of 836 mA mg<sup>-1</sup> in a broad potential range (0.2–0.6 V) for formic acid oxidation. The CO stripping experiment demonstrated its largely improved anti-CO poisoning ability with the peak potential of 0.67 V, approximately 60 and 40 mV less compared to those of Pd/GA-N and Pd/C samples. The high anti-CO poisoning ability and strong electronic effect resulting from the interaction between the 3D GA-N support and the Pd-Ni alloy makes it a promising catalyst for application in direct formic acid fuel cells

© 2020 Science Press Published by Elsevier B.V. All rights reserved.

#### 1. Introduction

Direct formic acid fuel cells (DFAFCs) as an important member of the proton exchange membrane fuel cells (PEMFC) family, have received increasing attention recently [1–3]. In the core part of the catalysts system, efficient catalysts for formic acid oxidation is very important to transfer the chemical energy to electrical energy. Pd-based catalysts are most commonly used because of the less poisoning problem during formic acid oxidation [4–6]. However, in such catalysts, the accumulation of poisoning species through long-term operation is unavoidable and can considerably decrease their catalytic performance [7,8]. High-performance catalysts with anti-poisoning ability are, therefore, urgently needed to advance fuel cell technology.

For the effective application in fuel cells, the active Pd species in the Pd-based catalyst must be uniformly dispersed over conductive supports such as active carbon to facilitate active site exposure and high stability [3,9]. The effect of several commercially available carbon materials on Pd catalyst for formic acid electrooxidation was studied, and it is found the carbon material is not only used

E-mail addresses: guangzhihu@ynu.edu.cn (G. Hu), ligang.feng@yzu.edu.cn (L. Feng).

as support but also involves the new active site formation resulting from the interaction of the Pd and Carbon support [10]. The increased conductivity and reduced charge transfer resistance are thus correspondingly observed [11,12]. Graphene, an allotrope of carbon, consists of a single layer of atoms arranged in a twodimensional honeycomb lattice with high chemical stability and ultra-high thermal conductivity; hence, graphene is ideal as a support for advanced Pd-based catalysts [13,14]. Several efforts have been undertaken to develop graphene-supported Pd catalysts for formic acid oxidation, and the property could be further impacted by heteroatom doping onto the carbon support or by oxophilic component hybridization in the catalyst system. For example, the electronic structures and chemical reactivity of N-doped graphene can be tuned, thereby enhancing the interaction between the active metal phase and graphene supports because of the easy adsorption of hydroxide ions (OH<sup>-</sup>) on the N site [15,16]. PdCu nanoparticles supported on the N-doped reduced graphene oxide showed enhanced activity toward formic acid oxidation due to the outstanding electron transfer capability and synergy between PdCu metallic and N-rGO support [17]. While the easy agglomeration and destruction of the pure graphene structure largely reduced their stability in performance maintenance [15]. Graphene aerogels (GAs), whose structure comprises 2D individual graphene sheets self-assembled to form 3D layers, could overcome the

<sup>\*</sup> Corresponding authors.

above-mentioned easy agglomeration and destruction problems. Thus, GAs are advantageous over pristine graphene, having the 2D structure, in terms of efficient ion and molecule transport and diffusion and large surface area [18,19]; thus, they might be a suitable support for advanced Pd-based catalysts. Moreover, oxophilicity is desirable in Pd-based catalysts because the easy generation of oxygen-containing species prevents the accumulation of poisoning intermediates [20,21]. The Pd-Ni alloy is an active phase for formic acid oxidation because of its anti-poisoning ability, which is improved by the oxophilicity of Ni [22,23]. Considering the above potential benefits, nitrogen doped GAs supported Pd-Ni active alloy would be a suitable platform for the formic acid oxidation. Though there are quite lots of Pd-Ni catalysts that have been reported in the traditional work, it is still not clear what will be obtained by combining the nitrogen-doped GAs and PdNi alloys.

Inspired by the above results, herein, we attempted to develop a catalyst that consisted of N-doped GAs (GA-N) and Pd-Ni nanoallov by a simple freeze-drying and the subsequent thermal annealing reduction approach. The Polyvinylpyrrolidone (PVP) used as the precursors was added to the mixture solution of GAs, Pd2+, Ni2+ and the freeze-dried solid material was thermally reduced in the N<sub>2</sub>/H<sub>2</sub> atmosphere. The as-prepared catalyst was studied for catalyzing formic acid oxidation. To our surprise and delight, though it did not show remarkably high catalytic current density for formic acid oxidation, an over wide potential activity (0.2-0.6 V) for formic acid oxidation was observed, that is rarely seen in the literature. To the best of our knowledge, only the WO<sub>2.72</sub>-nanorodsupported Pd catalyst was reported to have such catalytic activity over a wide potential range [24,25], which was attributed to the strong coupling effect between Pd and WO<sub>2.72</sub>. The catalytic activity for formic acid oxidation over a wide potential range also demonstrated its high anti-poisoning ability, which is highly appreciated in fuel cell technology. This catalytic ability might come from the high anti-CO poisoning ability and a strong electronic effect because of the interaction between the 3D GA-N support and the Pd-Ni alloy, and the catalytic performance-boosting will be necessary for the future study.

#### 2. Results and discussion

#### 2.1. Physical characterization

The synthetic procedure of Pd-Ni nanoparticles anchored on GA-N was shown in the schematic diagram, which included the freeze-dried solid material formation and the subsequent thermal annealing reduction of the freeze-dried solid material at 500 °C in H<sub>2</sub> atmosphere (Fig. 1a). This freeze-dried solid material included GAs, Pd<sup>2+</sup>, Ni<sup>2+</sup>, and PVP; the final catalyst powder thus obtained was denoted as PdNi/GA-N (see supporting information for details). The catalytic performance of PdNi/GA-N for formic acid oxidation was evaluated and compared to those of Pd/GA-N and Pd/C catalysts (Pd loading of 20 wt%). The crystalline structures of PdNi/GA-N, Pd/GA-N, and Pd/C were characterized by powder X-ray diffraction (XRD) analysis. The typical face-centered cubic (fcc) structure of Pd was observed for all samples in the XRD patterns (Fig. 1b). In particular, the three peaks at 40.1°, 46.6°, and 68.1° in Pd/GA-N and Pd/C, are assigned to the (111), (200), and (220) crystalline planes of Pd [26]. The main diffraction peaks of PdNi/GA-N are shifted to the higher  $2\theta$  values than those of the Pd/GA catalyst, indicating lattice contraction owing to the formation of a Pd-Ni alloy (PDF: 65-9444) [27]. The (002) facet of the carbon support is indicated by a broad peak at  $\sim 25^{\circ}$  for Pd/C and a sharp peak at 26° for the PdNi/GA-N and Pd/GA-N catalysts.

Furthermore, the morphology of the PdNi/GA-N catalyst was characterized by scanning electron microscopy (SEM) and trans-

mission electron microscopy (TEM). A hierarchical architecture structure with some pores in the graphene layer stacked in the 3D direction can be observed for PdNi/GA-N (Fig. 2a). Pd-Ni alloy particles are visible in the folding graphene surface in a magnified image (Fig. 2b). The interconnected 3D structure of PdNi/GA-N was confirmed by TEM images (Fig. S1). The dispersion of Pd-Ni alloy nanoparticles was clearly observed, and an average particle size of 5.4 nm was found from the histogram of the particle size distribution by counting 280 particles in a random TEM image (Fig. 2c and inset). The small particle size might be attributed to the addition of PVP, which suppresses the agglomeration of particles [28]. An interplanar spacing of 0.218 nm was observed in the highresolution TEM image, which can be corresponded to the (111) facet of the Pd-Ni alloy and a lattice fringe of 0.34 nm is visible from the graphene layer (Fig. 2d). The selected area electron diffraction (SAED) patterns clearly show the spots and rings indexed to the planes of Pd-Ni (111) in Fig. 2e. The EDX spectrum (Fig. 2f) confirms the presence of C, O, N, Ni, and Pd. The elemental distribution is shown in the element mapping images. Nitrogen is found uniformly doped into graphene, and several particles of Pd-Ni alloy are found on the graphene surface through randomly selected area of element mapping analysis (Fig. 2g-1).

#### 2.2. Electrochemical measurements

The electrochemical behavior of PdNi/GA-N, Pd/GA-N, and Pd/C was compared in a solution of 0.5 mol  $L^{-1}$   $H_2SO_4$ , and both polycrystalline Pd behaviors were observed with the hydrogen ad/desorption peaks and Pd oxide and reduction peaks and a flat double layer range (Fig. S2). The formic acid oxidation reaction of these catalysts was studied through cyclic voltammetry in 0.5 mol L<sup>-1</sup>  $\rm H_2SO_4$  and 0.5 mol  $\rm L^{-1}$  HCOOH (Fig. 3a). For formic acid oxidation, Pd/GA-N and Pd/C catalysts exhibited cyclic voltammetry profiles similar to those seen elsewhere [29,30]. Surprisingly, the profile of PdNi/GA-N was considerably different from that of the two other catalysts, with a high catalytic activity being observed over a wide potential range from 0.2 to 0.6 V, in place of an oxidation peak. Specifically, the mass activity in the anodic scan increases sharply to a near-maximum value at  $\sim 0.20$  V, which is maintained until the scanning potential reaches 0.60 V, after which the current drops sharply because of Pd oxidation [24]. Such a profile has only been reported in a few studies [31]. For example, hybrid support of HoO<sub>x</sub>/C supported Pd nanoparticles showed a high and stable current after the peak current because of the diminished poisoning effect from the oxidation intermediates. Such a catalytic activity in a broad potential range was recently found on the Pd/WO<sub>2.72</sub> system, resulting from the coupling effect induced the expansion of Pd lattice from 0.23 to 0.27 nm and decreased Pd surface electron density [24]. The catalytic activity for formic acid oxidation is retained over a very wide potential range and it could be attributed to the high resistance of PdNi/GA-N to CO poisoning. Moreover, the activity of a catalyst can be evaluated on the basis of its maximum mass activity. The PdNi/GA-N catalyst displays a high peak mass activity of 836 mA mg<sup>-1</sup>, which is 1.12 and 1.55 times higher than those of Pd/GA-N (746 mA mg<sup>-1</sup>) and Pd/C (537 mA mg<sup>-1</sup>), respectively. The mass activity of PdNi/GA-N is similar to that of Pd/GA-N; however, these catalysts have distinct profiles because of the compositional and electronic differences between Pd-Ni and GA-N-supported Pd (vide infra). The mass activity of PdNi/GA-N is also higher than or comparable to those of most recently reported Pd-based catalysts, though it is also inferior to some reports (Table S1), such as Pd<sub>1</sub>Ni<sub>1</sub>-NNs/RGO (604.3 mA mg<sup>-1</sup>) catalyst [22] and PdNiCu/C (792 mA mg<sup>-1</sup>) catalyst [5]. While we admitted that the catalytic activity judged by the maximum current was inferior to some of the advanced catalysts, that is probably because of the N-precursors of PVP adsorbed on

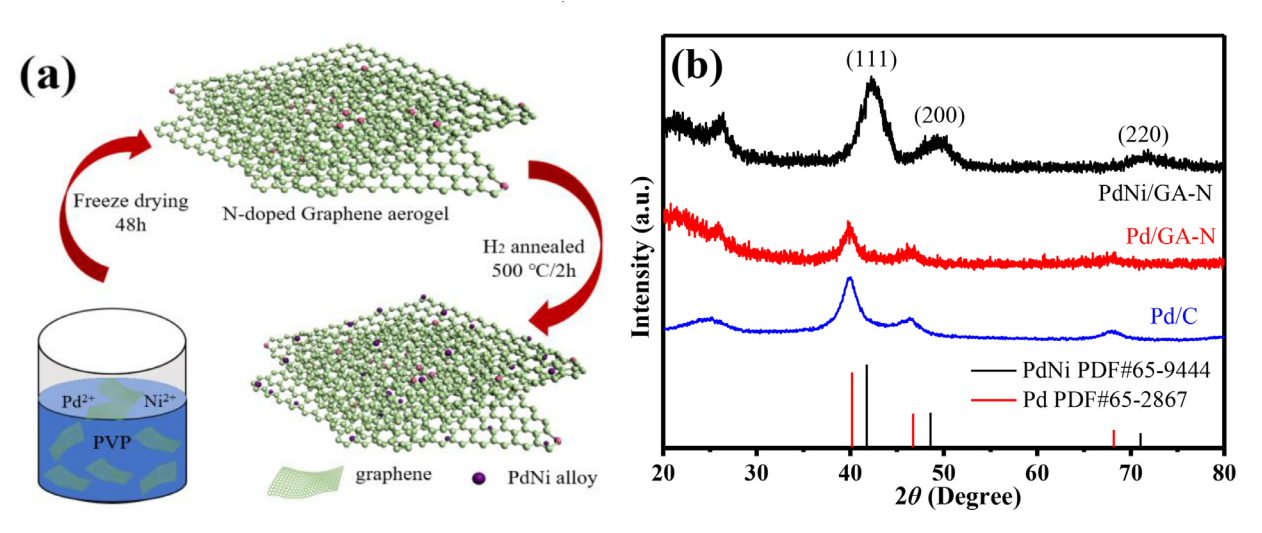


Fig. 1. (a) The synthetic procedure of PdNi/GA-N catalyst. (b) XRD patterns of PdNi/GA-N, Pd/GA-N and Pd/C catalysts.

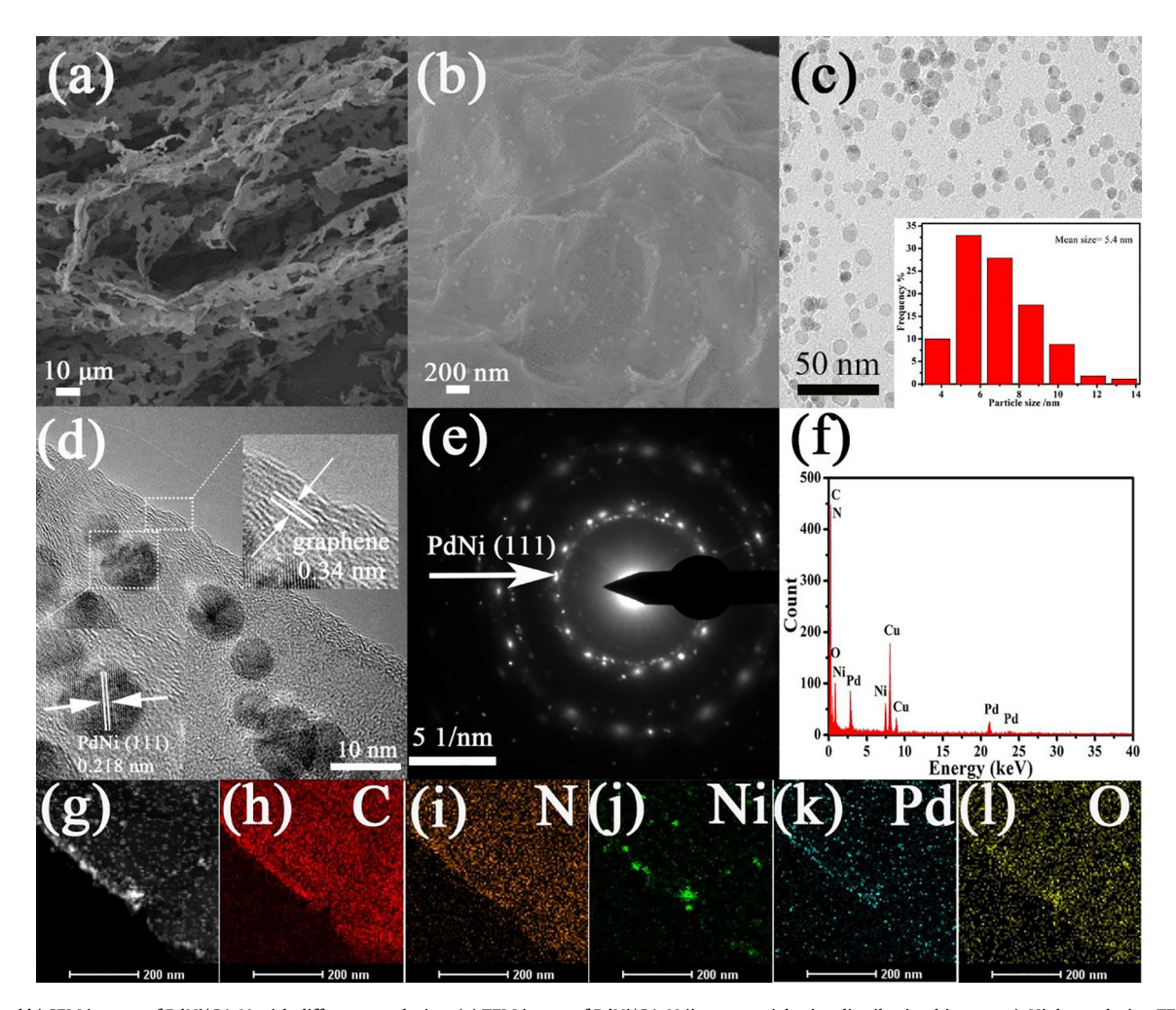


Fig. 2. (a and b) SEM images of PdNi/GA-N with different resolution. (c) TEM image of PdNi/GA-N (inset: particle size distribution histogram). High-resolution TEM (d), SAED (e) and EDX (f) of PdNi/GA-N. (g) STEM and elemental mapping images of the PdNi/GA-N catalyst, (h) C, (i) N, (j) Ni, (k) Pd, and (l) O.

the graphene or Pd surface, which reduced the exposure of the active site [32,33]. However, what we want to release is this catalyst that can offer the catalytic activity of formic aid oxidation in a wide potential range. To realize much higher catalytic perfor-

mance, future attention might be directed into the new approach for introducing the N elements. The stability of PdNi/GA-N, Pd/GA-N and Pd/C was compared by chronoamperometric (CA) experiments for 3600 s at a constant voltage of 0.1 V (Fig. 3b). The initial

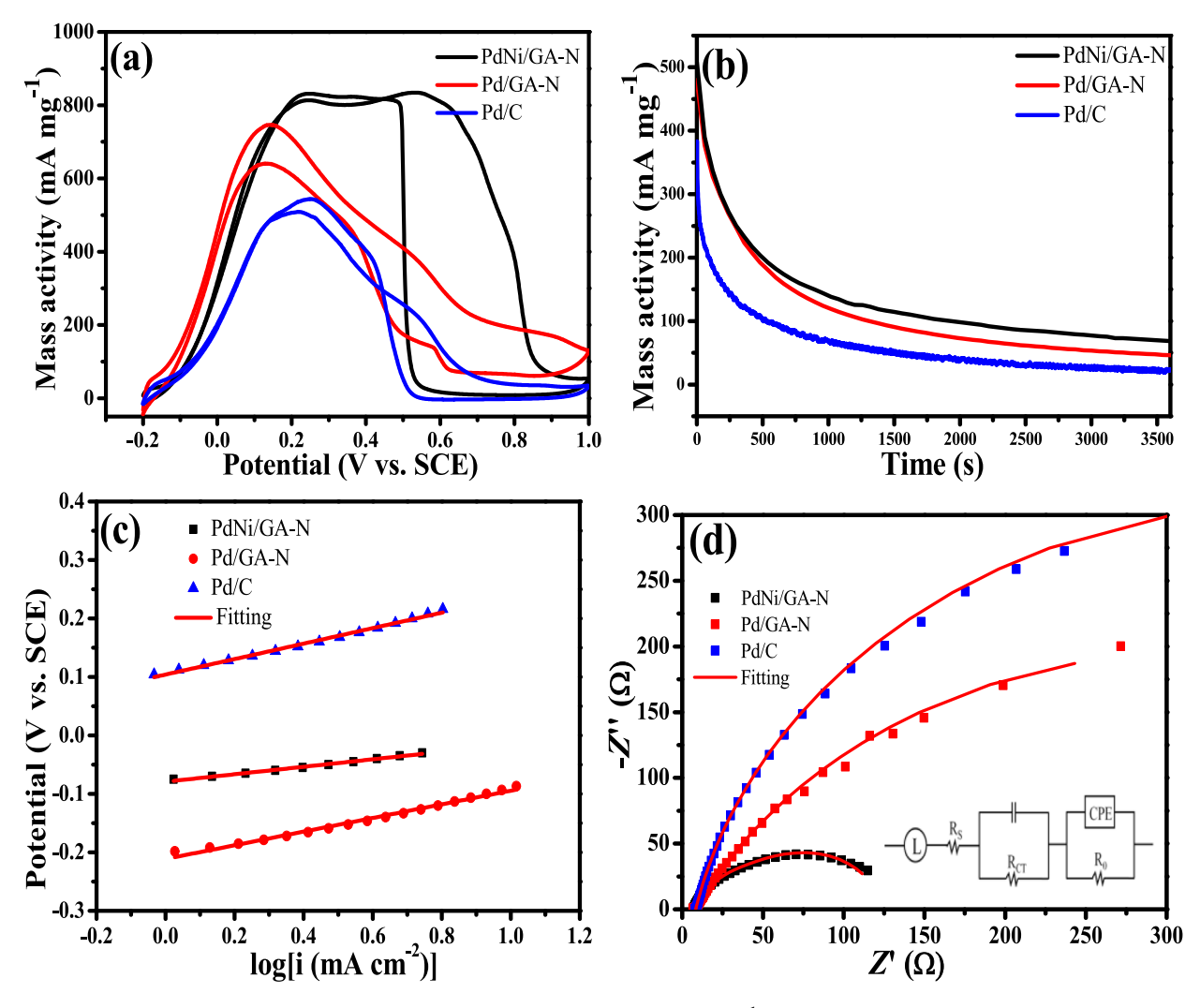


Fig. 3. (a) Cyclic voltammetry curves of PdNi/GA-N, Pd/GA-N and Pd/C catalysts at a scan rate of 50 mV·s $^{-1}$ . (b) Chronoamperometry curves of PdNi/GA-N, Pd/GA-N and Pd/C catalysts. (c) The corresponding Tafel plots for PdNi/GA-N, Pd/GA-N and Pd/C catalysts. (d) Nyquist plots of PdNi/GA-N, Pd/GA-N and Pd/C catalysts (inset of Fig. 3d: equivalent circuit). Electrolyte: 0.5 mol L $^{-1}$  H<sub>2</sub>SO<sub>4</sub>/0.5 mol L $^{-1}$  HCOOH solution; Pd loading: 0.08 mg cm $^{-2}$ .

mass activity of all catalysts decreased rapidly because of the double-layer charge effect, and thereafter, the activity was stable with time [34]. Specifically, the mass current density after 3600 s test was 69.2, 47.4 and 22.8 mA mg $^{-1}$  for PdNi/GA-N, Pd/GA-N and Pd/C, respectively. The value of PdNi/GA-N was as high as ca. 1.5 times for the pristine Pd/GA-N catalyst and 3.04 times of the Pd/C catalyst, indicating its outstanding capability to maintain the catalytic performance. To be specific, the activity loss during CA was normalized to the initial value to evaluate the performance decay rate. It was 76% for the PdNi/GA-N, much lower than those of Pd/GA-N (84%) and Pd/C (96%). The high ability to maintain the catalytic activity can be attributed to the high tolerance to the poisoning intermediates formed during the catalysis as discussed in the following CO stripping measurement.

To better understand the formic oxidation process, the well-accepted parallel mechanism for formic acid oxidation on the Pd catalyst was shown below. It includes two separated mechanisms, namely the formic acid is oxidized to CO<sub>2</sub> directly via the dehydrogenation pathway and the deteriorated dehydrogenation pathway where the poisoning intermediates species of CO is formed during the catalytic process [7].

```
Dehydrogenation pathway: HCOOH \rightarrow H^+ + e^- + HCOO^*
```

```
HCOO^* \rightarrow CO_2 + H^+ + e^-
Deteriorated dehydrogenation pathway:
HCOOH \rightarrow H^+ + e^- + HCOO^*
COOH^* \rightarrow CO^* + OH^*
CO^* + OH^* \rightarrow CO_2 + H^+ + e^-.
```

The catalytic mechanism can be reflected by the Tafel slope analysis. Here, the kinetic information for the electrooxidation of formic acid was acquired by quasi-static measurement through Tafel slope analysis. The Tafel slope of PdNi/GA-N was 63 mV dec<sup>-1</sup>, while those of Pd/GA-N and Pd/C were 116 and 132 mV  $dec^{-1}$ , respectively (Fig. 3c). The different values indicate the different catalytic mechanism for the rate-determining step. To be specific, the Tafel slope with a value of 60 mV dec<sup>-1</sup> indicates that the dehydrogenation process is the rate-determining step during  $CO_2$  formation [35], while the value of 120 mV dec<sup>-1</sup> indicates the first electron transfer in the breakage of C-H as the ratedetermining step [36,37]. The deviation from these typical values was generally observed and they can be attributed to factors such as solvent environment and the adsorption state of the electrocatalysts. Here, the Pd nanoparticles supported on the carbon or GA-N exhibited the Tafel slope close to the 120 mV dec<sup>-1</sup> resulting from the difficulty in the C-H bond splitting in the deteriorated dehydrogenation, while the catalytic rate-determining step was transformed to the direct CO<sub>2</sub> formation with the Tafel slope of

60 mV dec<sup>-1</sup>, which is desired for the reaction. Anyway, the smaller Tafel slope of PdNi/GA-N indicates a higher apparent electron transfer in the dominated catalysis step. Electrochemical impedance spectroscopy was conducted to study the charge transfer resistance for formic acid oxidation at 0.1 V (Fig. 3d). The parameters of uncompensated solution resistance  $(R_S)$  and charge transfer resistance  $(R_{CT})$  can be derived from the Nyquist plots with the help of data fitting by an equivalent circuit (inset of Fig. 3d). In the equivalent circuit, all physical components have a general meaning [38]. Specifically, no electrochemical process is involved for L of inductance from the external circuit,  $R_S$  and  $R_{CT}$  are for the uncompensated solution resistance and charge transfer resistance, and  $R_0$  stands for the contact resistance between the catalyst and the electrode, and two solid-phase elements (CPE) repents the double-layer capacitive property. The  $R_S$  value was  $\sim 6.8~\Omega$  for all electrodes, indicating their good electrode configuration in the same condition, while the lowest  $R_{\rm CT}$  value of 122  $\Omega$  was obtained for PdNi/GA-N, signifying its easiest and fastest charge transferability (Table S2).

The CV curves of PdNi/GA-N catalyst with different scan rates in 0.5 mol  $L^{-1}$  H<sub>2</sub>SO<sub>4</sub>/0.5 mol  $L^{-1}$  HCOOH solution was probed in Fig. 4a. With the increase of the scan rate, the mass activity of PdNi/GA-N catalyst was correspondingly increased and meanwhile, the catalytic activity over the wide potential was well maintained indicating the catalytic behavior was not influenced by the mass transfer but the intrinsic character. The CV curves at different scan rates for Pd/GA-N catalyst showed the conventional behaviors where the peak current was increased by increasing the scan rate (Fig. S3). The peak current  $(i_p)$  vs. the square root of scan rates (v) follows the equation of  $i_{\rm p}$  = 2.99  $\times$  105 $n(\alpha n')^{1/2}$   $AC_{\infty}D_0^{1/2}v^{1/2}$ , where the parameters have the general meaning in the supporting information. The slope for the relationship of the peak current and the scan rates is determined by the kinetics [39] (Fig. 4b), the larger slope of 25.93 obtained for PdNi/GA-N catalyst indicated its much faster electron-transfer ability in the rate-determining step than that of the Pd/GA-N catalyst with the slope of 19.76.

The improvement of catalytic ability is typically investigated on the basis of the electronic effect and the anti-poisoning ability during catalysis. Herein, X-ray photoelectron spectroscopy (XPS) was performed to examine the surface electronic state (Fig. 5a). The binding energy for the spectra was calibrated by the main peak of C 1s, referenced as 284.6 eV (Fig. S4a). The atomic contents of Pd and Ni on the surface were found to be 1.23% and 1.46%, respec-

tively, which is consistent with the nominal amounts (Table S3). The presence of N-doped graphene was confirmed by the C 1s and N 1s spectra corresponding to the C-N bond (Fig. S4a, b). Specifically, the N 1s spectra could be ascribed to the pyridinic N, pyrrolic N and graphitic N [40]. The Pd 3d spectrum could be separated into Pd  $3d_{5/2}$  and  $3d_{3/2}$  bands, and each band could be deconvoluted to Pd (0) and Pd (II) species [41]. Compared to Pd/ C, a positive shift of binding energy was found in both PdNi/GA-N and Pd/GA-N, indicating a strong electronic interaction between the active Pd species and the GA-N support. Meanwhile, a slightly higher positive shift was found for PdNi/GA-N compared to that for Pd/GA-N, which was consistent with the findings of previous reports on the Pd-Ni alloy [42,43]. It was proposed that the increase in the binding energy of Pd can be attributed to the higher number of band vacancies in Ni than that in Pd. which facilitated electron withdrawal from Pd. For all Pd spectra, metallic Pd dominated the surface composition, which promoted molecular adsorption and dissociation during formic acid oxidation (Table S4). The Ni 2p spectra have two bands corresponding to Ni  $2p_{3/2}$  and Ni  $2p_{1/2}$  (Fig. S4d), which can be attributed to metallic Ni (0), Ni (II), and the satellite peaks. Ni (II) is active for oxygen-containing species of Ni(OH)<sub>2</sub> and promotes NiOOH formation [44], thereby facilitating the removal of CO<sub>ad</sub> generated during formic acid oxidation based on the ligand effect.

This anti-poisoning ability is an essential property of a highperformance formic acid oxidation catalyst. Here, a CO-stripping experiment was carried out to examine the anti-CO poisoning ability and to estimate the number of active sites by the electrochemical active surface area (ECSA) (Fig. 5b). In the first scan, the absence of hydrogen desorption peaks at the lower potential region confirms the successful adsorption of CO on the catalytic surface, and then the CO oxidation peaks are observed on all the electrodes. The CO oxidation peak disappears in the subsequent second CV scan meanwhile the hydrogen desorption peak recovers indicating the complete oxidation removal of the adsorbed CO on the surface of the catalyst [8]. The lower the oxidation potential, the higher the CO<sub>ad</sub> oxidation ability and the higher the antipoisoning ability. Based on the onset and peak oxidation potentials of CO (Table S5), PdNi/GA-N exhibited the highest anti-CO poisoning ability. Pd/GA-N and Pd/C have similar onset potentials and peak potentials for CO oxidation, indicating similar catalytic mechanisms; while lower potentials for CO oxidation were observed for PdNi/GA-N, indicating the oxophilicity of Ni because of which oxy-

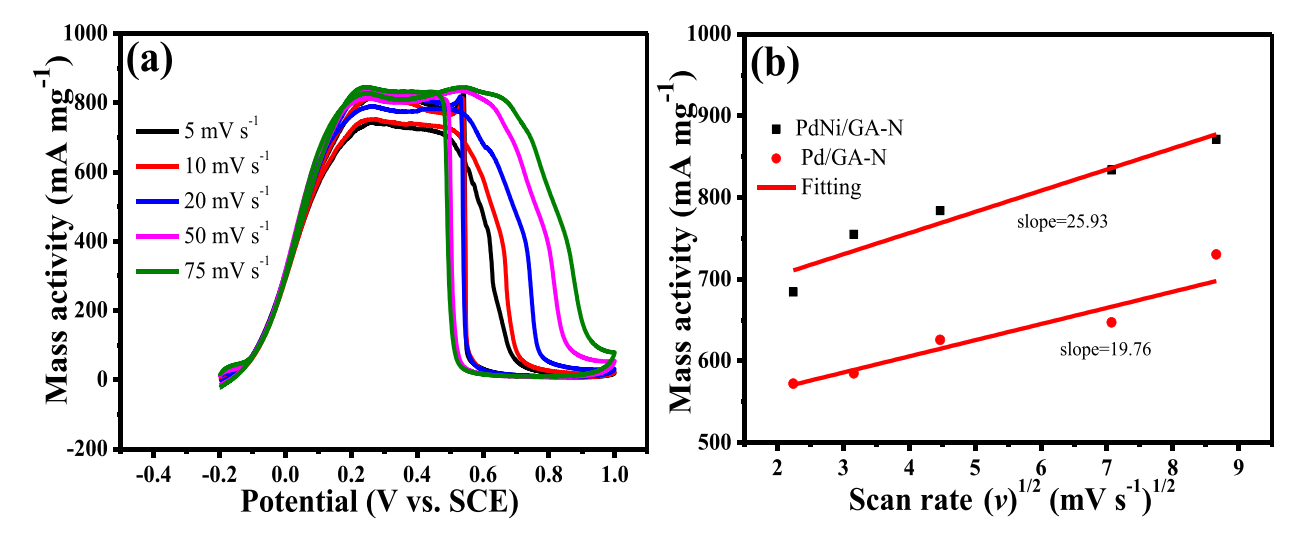


Fig. 4. (a) Cyclic voltammetry curves of PdNi/GA-N catalyst at different scan rates. (b) The relationship between the peak current and the square root of scan rates of PdNi/GA-N and Pd/GA-N catalysts.

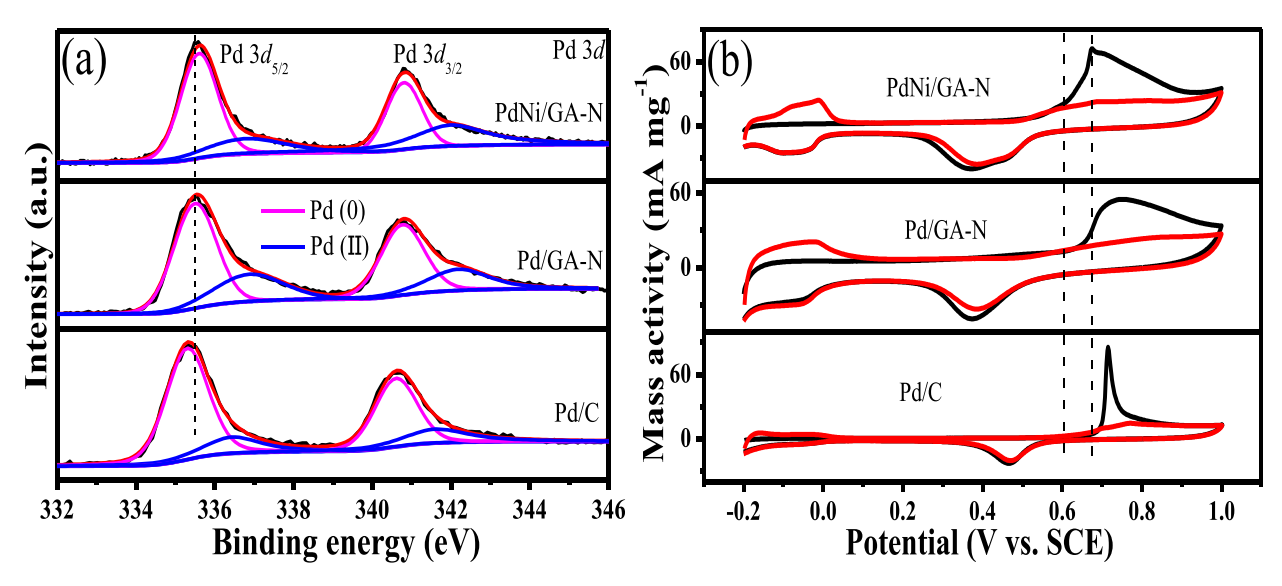


Fig. 5. (a) XPS spectra of Pd 3d for PdNi/GA-N, Pd/GA-N and Pd/C catalysts. (b)  $CO_{ad}$  stripping voltammograms of PdNi/GA-N, Pd/GA-N and Pd/C in 0.5 mol  $L^{-1}$  H<sub>2</sub>SO<sub>4</sub> solution at the scan rate of 20 mV s<sup>-1</sup>

gen species are offered for CO oxidation via the bi-functional catalytic mechanism [45]. Specifically, the CO oxidation peak potential was 0.67 V for PdNi/GA-N, approximately 60 and 40 mV lower than those of Pd/GA-N and Pd/C, respectively. When evaluated by the onset potential of the CO oxidation, it was 50 mV and 90 mV less than those of Pd/GA-N (0.65 V) and Pd/C (0.69 V) catalysts. The ECSA of PdNi/GA-N, Pd/GA-N, and Pd/C was calculated to estimate the active sites, which were  $\sim 75$ , 68, and 56 m² g $^{-1}$ , respectively. The larger ESCA indicated good dispersion of Pd–Ni and Pd nanoparticles over the GA-N support, thereby facilitating active site exposure as well as catalyst performance improvement. Here it could be concluded that the PdNi/GA-N catalyst exhibited largely improved anti-CO poisoning ability, which was helpful for the high activity for formic acid oxidation over a wide potential range.

#### 3. Conclusion

In summary, we found that PdNi/GA-N prepared by a simple freeze-drying and thermal annealing H<sub>2</sub> reduction approach exhibited catalytic ability for formic acid oxidation over a wide potential range. The Pd-Ni alloy particles were found anchoring over the folding N-doped graphene surface with a porous hierarchical architecture structure. Specifically, it showed the catalytic performance with its maximum mass activity of 836 mA mg<sup>-1</sup> in a broad potential range (0.2-0.6 V). PdNi/GA-N was also found to have improved catalytic kinetics and appreciated catalytic mechanism for formic acid oxidant. This unexpected catalytic behavior was rarely seen in the literature which is worthy of further study. This catalyst exhibited high anti-CO poisoning ability and a strong electronic effect because of the interaction between the 3D GA-N support and the Pd-Ni alloy. The over wide catalytic activity and antipoisoning ability make PdNi/GA-N a promising catalyst for formic acid oxidation in fuel cell technology.

#### **Declaration of Competing Interest**

The authors declare that they have no known competing financial interests or personal relationships that could have appeared to influence the work reported in this paper.

#### Acknowledgements

The work is supported by the National Natural Science Foundation of China (21972124, 21603041), a project funded by the Priority Academic Program Development of Jiangsu Higher Education Institution, the Double Tops Joint Fund of the Yunnan Science and Technology Bureau and Yunnan University (2019FY003025) and the Research Foundation of Department of Education of Yunnan Province (2020Y0018).

#### Appendix A. Supplementary data

Supplementary data to this article can be found online at https://doi.org/10.1016/j.jechem.2020.12.007.

#### References

- [1] T. Shen, J. Zhang, K. Chen, S. Deng, D. Wang, Energy Fuel 34 (2020) 9137–9153.
- [2] M. Choi, C.-Y. Ahn, H. Lee, J.K. Kim, S.-H. Oh, W. Hwang, S. Yang, J. Kim, O.-H. Kim, I. Choi, Y.-E. Sung, Y.-H. Cho, C.K. Rhee, W. Shin, Appl. Catal. B: Environ. 253 (2019) 187–195.
- [3] Y. Ma, T. Li, H. Chen, X. Chen, S. Deng, L. Xu, D. Sun, Y. Tang, J. Energy Chem. 26 (2017) 1238–1244.
- [4] Y. Chen, Y. Yang, G. Fu, L. Xu, D. Sun, J.-M. Lee, Y. Tang, J. Mater. Chem. A 6 (2018) 10632–10638.
- [5] L. Feng, J. Chang, K. Jiang, H. Xue, C. Liu, W.-B. Cai, W. Xing, J. Zhang, Nano Energy 30 (2016) 355–361.
- [6] L. Liang, F. Vladimir, J. Ge, C. Liu, W. Xing, J. Energy Chem. 37 (2019) 157–162.
- [7] K. Jiang, H.-X. Zhang, S. Zou, W.-B. Cai, Phys. Chem. Chem. Phys. 16 (2014) 20360–20376.
- [8] Y. Bao, H. Liu, Z. Liu, F. Wang, L. Feng, Appl. Catal. B: Environ. 274 (2020) 119106.
  [9] M.F.R. Hanifah, J. Jaafar, M.H.D. Othman, A.F. Ismail, M.A. Rahman, N. Yusof, F.
- Aziz, N.A.A. Rahman, J. Alloys Compd. 793 (2019) 232-246.
- [10] J. Chang, S. Li, L. Feng, X. Qin, G. Shao, J. Power Sour. 266 (2014) 481–487.
  [11] T. Szumełda, A. Drelinkiewicz, E. Lalik, R. Kosydar, D. Duraczyńska, J. Gurgul, Appl. Catal. B: Environ. 221 (2018) 393–405.
- [12] A. Caglar, M.S. Cogenli, A.B. Yurtcan, H. Kivrak, Renew. Energ. 150 (2020) 78–90.
- [13] X. Yu, C. Pei, L. Feng, Chin. Chem. Lett. 30 (2019) 1121-1125.
- [14] F. Yang, B. Zhang, S. Dong, C. Wang, A. Feng, X. Fan, Y. Li, J. Energy Chem. 29 (2019) 72–78.
- [15] X. Zhang, J. Zhu, C.S. Tiwary, Z. Ma, H. Huang, J. Zhang, Z. Lu, W. Huang, Y. Wu, ACS Appl. Mater. Interfaces 8 (2016) 10858–10865.
- [16] F. Razmjooei, K.P. Singh, D.-S. Yang, W. Cui, Y.H. Jang, J.-S. Yu, ACS Catal. 7 (2017) 2381–2391.
- 17] S.R. Chowdhury, T. Maiyalagan, Int. J. Hydrog. Energy 44 (2019) 14808-14819.
- [18] X. Zhang, Y. Han, L. Huang, S. Dong, ChemSusChem 9 (2016) 3049-3053.
- [19] H. Liu, D. Yang, Y. Bao, X. Yu, L. Feng, J. Power Sour. 434 (2019) 226754.

- [20] X. Liu, Y. Bu, T. Cheng, W. Gao, Q. Jiang, Electrochim. Acta 324 (2019) 134816.
- [21] Y. Zhou, D. Liu, Z. Liu, L. Feng, J. Yang, ACS Appl. Mater. Interfaces 12 (2020) 47065–47075.
- [22] D. Bin, B. Yang, F. Ren, K. Zhang, P. Yang, Y. Du, J. Mater. Chem. A 3 (2015) 14001–14006.
- [23] Y. Jin, J. Zhao, F. Li, W. Jia, D. Liang, H. Chen, R. Li, J. Hu, J. Ni, T. Wu, D. Zhong, Electrochim. Acta 220 (2016) 83–90.
- [24] Z. Xi, J. Li, D. Su, M. Muzzio, C. Yu, Q. Li, S. Sun, J. Am. Chem. Soc. 139 (2017) 15191–15196.
- [25] Z. Xi, D.P. Erdosy, A. Mendoza-Garcia, P.N. Duchesne, J. Li, M. Muzzio, Q. Li, P. Zhang, S. Sun, Nano Lett. 17 (2017) 2727–2731.
- [26] L. Sun, B. Liao, X. Ren, Y. Li, P. Zhang, L. Deng, Y. Gao, Electrochim. Acta 235 (2017) 543–552.
- [27] E. Lohrasbi, M. Javanbakht, S.A. Mozaffari, Ind. Eng. Chem. Res. 55 (2016) 9154–9163.
- [28] Z. Daşdelen, Y. Yıldız, S. Eriş, F. Şen, Appl. Catal. B: Environ. 219 (2017) 511–516.
- [29] X. Liang, B. Liu, J. Zhang, S. Lu, Z. Zhuang, ChemComm 52 (2016) 11143-11146.
- [30] J. Shan, T. Zeng, W. Wu, Y. Tan, N. Cheng, S. Mu, Nanoscale 12 (2020) 12891–12897.
- [31] L. Feng, X. Sun, C. Liu, W. Xing, ChemComm 48 (2012) 419-421.
- [32] T. Wang, R. Yang, S. Ouyang, H. Shi, S. Wang, RSC Adv 5 (2015) 48992–48996.

- [33] N.V. Long, M. Ohtaki, M. Nogami, T.D. Hien, Colloid Polym. Sci. 289 (2011) 1373-1386.
- [34] X. Yang, J. Xue, L. Feng, ChemComm 55 (2019) 11247-11250.
- [35] Y. Wang, Q. He, H. Wei, J. Guo, K. Ding, Q. Wang, Z. Wang, S. Wei, Z. Guo, Electrochim. Acta 184 (2015) 452–465.
- [36] H. Wang, L. Alden, F.J. DiSalvo, H.D. Abruña, Phys. Chem. Chem. Phys. 10 (2008) 3739–3751.
- [37] J.D. Lović, A.V. Tripković, S.L. Gojković, K.D. Popović, D.V. Tripković, P. Olszewski, A. Kowal, J. Electroanal. Chem. 581 (2005) 294–302.
- [38] F. Wang, H. Xue, Z. Tian, W. Xing, L. Feng, J. Power Sour. 375 (2018) 37–42.
- [39] G. Li, L. Feng, J. Chang, B. Wickman, H. Grönbeck, C. Liu, W. Xing, ChemSusChem 7 (2014) 3374–3381.
- [40] C. Pei, R. Ding, X. Yu, L. Feng, ChemCatChem 11 (2019) 4617-4623.
- [41] E.J. Lim, H.J. Kim, W.B. Kim, Catal. Commun. 25 (2012) 74-77.
- [42] C. Xu, Y. Liu, Q. Hao, H. Duan, J. Mater. Chem. A 1 (2013) 13542.
- [43] L. Leng, J. Li, X. Zeng, H. Song, T. Shu, H. Wang, S. Liao, J. Power Sour. 337 (2017) 173–179.
- [44] K. Zhang, H. Xu, B. Yan, J. Wang, Y. Du, Q. Liu, Electrochim. Acta 268 (2018) 383–391.
- [45] S. Wang, J. Chang, H. Xue, W. Xing, L. Feng, ChemElectroChem 4 (2017) 1243– 1249.